Photo-Fenton degradation of methylene blue using hematite-enriched slag under visible light

ALI, Ahmed, KHAN, Irfan, ZHANG, Bofan, NOMURA, Kiyoshi, HOMONNAY, Zoltan, KUZMANN, Erno, SCRIMSHIRE, Alex, BINGHAM, Paul <http://orcid.org/0000-0001-6017-0798>, KREHULA, Stjepko, MUSIC, Svetozar, AKIYAMA, Kazuhiko and KUBUKI, Shiro

Title page

Names of the authors:

Ahmed S. Ali[1], Irfan Khan[1], Bofan Zhang[1], Kiyoshi Nomura[1], Zoltan Homonnay[2], Erno Kuzmann[2], Alex Scrimshire[3], Paul A Bingham[3], Stjepko Krehula[4], Svetozar Musić[4], Kazuhiko Akiyama[1], Shiro Kubuki[1]

Title: Photo-Fenton degradation of methylene blue using hematite-enriched slag under visible light

Affiliations and addresses of the authors:

[1] Department of Chemistry, Graduate School of Science and Engineering, Tokyo Metropolitan University, 1-1 Minami-Osawa, Hachi-Oji, Tokyo 192-0397, Japan

[2] Institute of Chemistry, Eötvös Loránd University, Pázmány P. s. 1/A, Budapest, 1117, Hungary

[3] Materials and Engineering Research Institute, Faculty of Science, Technology and Arts, Sheffield Hallam University, Howard Street, Sheffield S1 1WB, UK

[4] Division of Materials Chemistry, Ruđer Bosković Institute, Bijenička c. 54, 10000 Zagreb, Croatia

E-mail address of the corresponding author: Balasfora2000@yahoo.com

Photo-Fenton degradation of methylene blue using hematite-enriched slag under visible light

Ahmed S. Ali[1], Irfan Khan[1], Bofan Zhang[1], Kiyoshi Nomura[1], Zoltan Homonnay[2], Erno Kuzmann[2], Alex Scrimshire[3], Paul A Bingham[3], Stjepko Krehula[4], Svetozar Musić[4], Kazuhiko Akiyama[1], Shiro Kubuki[1]

[1] *Department of Chemistry, Graduate School of Science and Engineering, Tokyo Metropolitan University, 1-1 Minami-Osawa, Hachi-Oji, Tokyo 192-0397, Japan*

[2] *Institute of Chemistry, Eötvös Loránd University, Pázmány P. s. 1/A, Budapest, 1117, Hungary*

[3] *Materials and Engineering Research Institute, Faculty of Science, Technology and Arts, Sheffield Hallam University, Howard Street, Sheffield S1 1WB, UK*

[4] *Division of Materials Chemistry, Ruđer Bosković Institute, Bijenička c. 54, 10000 Zagreb, Croatia*

Abstract:

This study aims to find a suitable method to transform the amorphous iron oxides obtained from the incineration of combustible waste slag (CWS) into hematite. The resulting samples were utilized as heterogeneous photocatalysts for the photo-Fenton degradation of methylene blue (MB) aqueous solution. A good correlation was found between the MB degradation and the amount of hematite phase as confirmed by XRD and Mössbauer measurements. The largest rate constant (k) was $(4.1 \pm 0.08) \times 10^{-2}$ min^{-1} for MB decomposition under visible-light for the sample N5-50-800. The results are promising for both low-cost photocatalysts and recycling of combustible waste slags.

Article highlights

- A facile method for slag management into photocatalyst is presented
- The key component for degradation was the formation of hematite after heat-treatment
- Hematite was confirmed using XRD and Mössbauer techniques

Keywords visible-light activated photocatalytic effect; photo-Fenton reaction; slag; Hematite iron oxide; ^{57}Fe-Mössbauer spectroscopy

1. Introduction

Among many problems in our world today, two major problems grab the attention of scientists and the public alike: combustible wastes, leading to scarcity of landfill and need to find new recycling and circular economy approaches; and wastewater pollution. With an increasing the world population, these two problems are becoming increasingly serious unless more effective steps are taken [1].

For combustible wastes, many countries have established waste incineration or waste-to-energy (WTE) plants to meet the lack of landfill whilst generating useful energy, although the by-products from such processes (ashes and slags) can themselves present both hazards and opportunities [2].

There are predominantly two types of slag; firstly, industrial slags which are produced during ferrous and non-ferrous smelting processes. The smelting of copper, lead and bauxite in non-ferrous smelting is designed to remove the iron and silica that often occurs with those ores and separates them as iron-silicate-based slags [3]. On the other hand, ferrous smelting in steel mills is designed to minimize iron loss so these slags mainly consist of oxides of calcium, silicon, magnesium and aluminium. Secondly, there are combustible waste slags (CWS) such as those produced by combustible waste incineration and waste-to-energy (WTE) plants. Such wastes are incinerated at temperatures of ca. 800°C, which reduces the volume to 1/20 of its original volume [4].

The compositions of CWS are similar to iron-containing silicate glasses, for which the photocatalytic effect has previously been observed [5]. To date, CWS is used in civil engineering works as a low-value base material or aggregate for the construction of roads and concretes so new applications and new opportunities for valorization and recycling of CWS is essential from both economic and environmental perspectives.

For wastewater, several techniques have been applied for the treatment of wastewater effluents. Among these, photocatalysis is one of the most environmentally friendly approaches. The most commonly-applied photocatalyst is TiO_2, which shows photocatalytic activity under UV light due to its wide bandgap of 3.2 eV [6]. This wide bandgap limits the practical uses of TiO_2 as UV light is only available from solar irradiation as a small percentage, ca. 5%, compared to visible light, ca. 40% [7]. Iron oxides, mainly hematite (Fe_2O_3) are promising alternatives due to their lower bandgap around 2.3 eV, low cost, chemical stability and comparatively environmentally friendly nature. Moreover, applying the Fenton reaction and the light-accelerated Fenton reaction, commonly known as the photo-Fenton reaction, provides an added value for using iron oxides as photocatalysts [8].

Iida et al. [9] reported that iron alumino-silicate glass, $15Na_2O{\cdot}15CaO{\cdot}40Fe_2O_3{\cdot}11Al_2O_3{\cdot}19SiO_2$ (weight %), which has a similar composition to CWS, showed a photocatalytic effect after heat treatment at 1000 °C for 100 min, with a k (pseudo-first-order rate constant) of 9.26×10^{-3} min^{-1} for MB degradation. Ishikawa et al. [5] reported that heat treatment of waste slag recycled glass-ceramics (WSRG) with additional Fe_2O_3 content of 10, 30 and 50 mass% decomposed MB aqueous solution with first-order rate constants (k) of 2.6, 2.3 and 2.7×10^{-3} min^{-1}, respectively, under visible light irradiation. The degradation was related to the precipitated amount of α-Fe_2O_3 nanoparticles. Khan et al. [10] also prepared iron-containing aluminosilicate glass by a sol-gel method, which provided a k value of 8.61×10^{-2} min^{-1} in the photo-Fenton degradation of MB, where the amount of precipitated hematite was increased by the introduction of Al_2O_3.

In our previous work [11], we succeeded in preparing glass and glass-ceramics from CWS by melt-quenching, obtaining k values of up to 2.2×10^{-2} min^{-1} by melting the slag at 1400 °C, then subsequently heat treating it at 800 °C for 100 min. Here we aim to

enhance the results achieved by melt quenching by introducing a facile method for using DSW as a photocatalytic material by treating as-collected DSW with HNO_3 and applying the photo-Fenton reaction under visible light irradiation. The proposed method depends on treating as-collected CWS with nitric acid at room temperature, which could further reduce costs since no high preparation temperatures are required.

Reacting nitric acid with CWS compositions, which are mainly metal oxides, will release the metals from the slag matrix in the form of nitrate salts. Iron oxide, Fe_2O_3, as one of these oxides, will convert to iron nitrate which decomposes at high temperatures, through a series of reactions, to form hematite, α-Fe_2O_3 [12], one of the iron oxides used as a visible-light photocatalyst. If some levels of $Fe(NO_3)_3$ persist after heat treatment, it will increase the degradation [13]. There is little literature concerning the acid treatment of CWS. Most related studies have used acid treatment for metals recovery from smelting slags or for neutralizing the acid by adding basic slags. For example, Akcil et al. [14] used nitric acid for the recovery of rare earth metals and production of precipitated silicon dioxide from phosphorus slag which contains inorganic oxides similar to CWS. They used concentrated nitric acid (7.0 – 7.5 M) and slag to acid ratio S: L = 1.0:2.6 at a temperature of 90 °C for 1 hour. Nitric acid was also used for extracting soluble phosphorus from slag with high P_2O_5 content by selective leaching. When nitric acid was used, 66.8% of the solid solution was dissolved [15]. Some researchers have studied photoactivity using metallurgical slag combined with TiO_2, CdO/graphene or other materials, however, some drawbacks exist as some use UV light [16-18], long irradiation times (e.g. 300 min) [19], or low pH (e.g. 3) [20].

In this work, the relationship between the visible-light activated catalytic effect and local structure of the slag treated by nitric acid was, for the first time, investigated by ^{57}Fe-Mössbauer spectroscopy, X-ray diffraction (XRD), transmission electron microscopy (TEM) and optical absorption spectroscopy (UV-Vis).

2. Experimental Procedures

2.1. Materials

The slag used in this study was collected in July 2018 at the Tamagawa municipal waste combustion plant (Ohta-ku, Tokyo, Japan) according to the agreement between Tamagawa municipal waste combustion plant and faculty of science - Tokyo metropolitan university. Chemical reagents of Nitric acid HNO_3 (13M CAS No. 141-01361), hydrogen peroxide 30% (H_2O_2: CAS No. 081-04215) and methylene blue (MB: $C_{16}H_{18}N_3SCl_3 \cdot H_2O$, CAS No. 133-06962) were purchased from Wako, Japan.

2.2. Sample preparation

The as-collected slag was pulverized using an electric agate mortar and the XRF compositional analysis is presented in Table 1. As one of the important parameters affecting the dissolution rates, the ratio of slag/acid is very important [21], several ratios were prepared to study the effect of HNO_3 amount on the structure and photocatalytic ability. One gram of pulverized slag was added to different amounts (20, 10, 5 and 3 ml) of concentrated HNO_3 in a glass beaker and stirred at room temperature. The time required for full dissolution of the slag decreased with the amount of HNO_3. During the dissolution process, black orange fumes were liberated so the whole experiment was performed in an extraction hood. After the dissolution of the slag was complete, a green-coloured solution was obtained. The solution was then directly moved to a dryer at 80 °C in Petri dishes with thickness 2-3 mm, and held for 24 h. Over this period the colour changed from greenish to dark orange, consistent with the change in the iron oxide oxidation state from Fe^{2+} to Fe^{3+}, which was confirmed by ^{57}Fe Mössbauer measurements as shown in section 3.1.2. The dried samples were pulverized and heat-treated at 1000 °C according to the thermal gravimetric analysis (TG) results (see Fig. 1) at a heating rate of 5 °C/min and the resulting samples are thus denoted N20-1000, N10-1000, N5-1000 and N3-1000. For the samples prepared using dilute HNO_3, the same route was followed by adding additional amounts of distilled water as shown in Table 2. The preparation route is presented in scheme 1. The samples were denoted according to the percentage volume of

HNO_3 to the total volume of the solution and the heat treatment temperature. For example, N5-75-800 means that for one gram of slag, the total volume of the solution is 5 ml while the HNO_3 volume is 75% and the heat treatment temperature is 800 °C. The sample of 25% HNO_3 content did not fully dissolve so we obtained two samples, N5-75 and N5-50, which were heat-treated at 800 and 1000 °C.

2.3. Characterization techniques

Sample structure before and after heat treatment were characterized by ^{57}Fe Mössbauer spectroscopy, X-ray diffractometry (XRD), Scanning electron microscopy (SEM), Transmission electron microscopy (TEM) and the Brunauer-Emmett-Teller (BET) specific surface area analysis. ^{57}Fe Mössbauer spectra were measured using a constant acceleration spectrometer. A source of 925 MBq ^{57}Co (Rh) was attached to an MVT-1000 transducer connected to an MDU-1200 drive unit. The drive unit was connected to a DFG-1200 digital function generator with 1200 channels. Transmitted γ-rays were detected by a proportional counter. The signals were amplified by an ORTEC 142 preamplifier. The applied voltage (2 kV) was obtained by using an ORTEC 556 High voltage–power supply, and an ORTEC 570 amplifier. The amplified signals were monitored with a PC via an ORTEC EASYMSC. Samples with weight = 40 mg were homogeneously dispersed in a circular sample holder with 10 mm diameter; inserted into the spectrometer, and measured until the total counts collected were greater than 10^6. Isomer shifts are given relative to α-Fe, which was measured as a reference. The Mösswinn 3.0i XP software was used to analyze the obtained spectra. XRD patterns were recorded using a RINT TTR3, Rigaku diffractometer between 2θ of 10° to 80°, with precision and scan rates of 0.02 and 5°/ min, respectively. Cu-Kα X-rays (λ = 0.1541 nm) were generated at 50 kV and 300 mA, and monochromated. SEM images were taken by Keyence VE 9800 with the applied voltage of 2 kV, and magnification of 2000x. TEM images were obtained using a JEM-3200FS Field Emission Energy Filter Electron Microscope. The Brunauer-Emmett-Teller (BET) specific surface area was estimated from N_2 isotherms obtained using a BELSORP mini II (BEL Japan, Osaka, Japan) at 77 K. The analyzed samples were evacuated at 573 K for 3 h before each measurement.

198

199 2.4. Photo-Fenton Reaction

200 For the evaluation of photocatalytic properties, we used 40 mg of pulverized sample
201 and 10 mL of methylene blue aqueous solution (MB_{aq}) with an initial concentration of
202 20 μmol L^{-1}. Additional amounts of hydrogen peroxide (9.79 M) (Wako: 081-04215 30%
203 mass/mass) was added to the MB solution. UV–Vis optical absorption spectra of the MB
204 solution before and after the photocatalytic reaction test were measured from the
205 absorbance of the peak at 665 nm, using a GENESYS™ 10S UV-Vis spectrophotometer.
206 The light was emitted by a metal-halide lamp with output wavelengths from 420 to
207 750 nm, an output power of 100 W and an intensity of 6 mW cm^{-2}, with the distance
208 between the sample and the light source maintained at 20 cm, and a UV filter was used.
209 All samples were also measured in the dark to investigate the effect of adsorption as a
210 control. All measurements were performed at room temperature.

211

212 3. Results and discussion

213 3.1. Structural characterization

214 3.1.1 XRD

215 Figure 2(a) shows the XRD patterns for the samples dissolved in concentrated HNO_3
216 heat-treated at 1000 °C for 100 min. The samples N20, N10 and N5 show crystalline
217 peaks ascribed to hematite (Fe_2O_3, PDF No. 01-089-0598), gehlenite (Ca_2Al (Al Si) O_7,
218 PDF No. 01-089-5917) and esseneite ($CaFe_{0.6}Al_{1.34}Si_{1.08}O_6$, PDF No. 01-084-1206). The
219 sample N3 does not evidence peaks related to hematite but shows peaks consistent with
220 gehlenite and esseneite, with the same PDF numbers previously mentioned. This sample
221 also produces diffraction peaks attributed to Andradite ($Ca_3Fe_2O_{12}Si_3$, PDF No. 01-084-
222 1206). The intensity of hematite peaks decreases, with decreasing HNO_3 addition from 20
223 to 5 ml for the samples N20 to N5, respectively. These results indicate that the amount of
224 HNO_3 has a large impact on the development of the hematite phase obtained from heat-
225 treatment. Since hematite is known as a visible light photocatalyst, it was expected that
226 the sample N20 would produce the highest MB_{aq} degradation values due to the existence

of hematite as the most prominent phase. It was also expected that the MB_{aq} degradation of the samples N10, N5 and N3 would decrease gradually due to the gradual decrease in hematite content. It should be noted that in our previous work [11], we could not detect any XRD peaks related to hematite in the slag after melting at 1400 °C and heat-treatment at 800 °C for 100 min unless Fe_2O_3 additions were made to increase the Fe_2O_3 content of the resulting material to 50%. Figure 2(c) shows the XRD pattern of the slag (same slag used in this study), melted at 1400 °C and heat-treated at 800 °C for 100 min. The identified phases are iron silicon oxide ($Fe_{2.95}Si_{0.05}O_4$, PDF No. 00-052-1140) and calcium silicate (Ca_2SiO_4, PDF No. 00-024-0234). This means that dissolving the slag in HNO_3 can produce hematite without the requirement for additional Fe_2O_3, leading to better degradation results and simpler production.

Figure 2(b) shows the XRD patterns for the samples dissolved in dilute HNO_3 (75 and 50%) after heat treatment at 800 and 1000 °C for 100 min, respectively. Clear diffraction peaks can be detected for gehlenite (Ca_2Al (Al, Si) O_7, PDF No. 01-089-5917), hematite (Fe_2O_3, PDF No. 01-089-0596) and andradite (Ca_3Fe_2 $(SiO_4)_3$, PDF No. 01-084-1935) for all samples. Heat treatment at 1000 °C for both N5-75 and N5-50 samples increased their crystallinity as demonstrated by the narrower diffraction peaks compared to those obtained in the corresponding samples heat-treated at 800 °C, suggesting that the crystallite size increased as the temperature increased, which is also reflected in the measured surface area. Also, the intensity of hematite peaks decreased while the intensity of gehlenite peaks increased for heat treatment at 1000 °C compared to 800 °C. It is thus concluded that HNO_3 concentration plays a major role in controlling the obtained phases while heat treatment temperature affects the phase distribution and the crystallite size. These results are consistent with that obtained from Mössbauer spectra.

3.1.2 Mössbauer Spectroscopy

3.1.2.1 Mössbauer spectroscopy of slag dissolved in concentrated HNO_3

The as-collected slag spectra and fitted data, in Fig. 4(c) and Table 3, show two paramagnetic doublets with δ = 1.01 $\pm$ 0.01 mm s^{-1} and 0.48 $\pm$ 0.06 mm s^{-1} related to

Fe^{II} O_h and Fe^{III} O_h, respectively. The spectra and parameters for all samples prepared using concentrated HNO_3 after heat treatment at 1000 °C for 100 min are shown in Fig. 3 and Table 3, respectively. The spectra of the samples N20, N10 and N5 exhibit two doublets related to Fe^{III} and one sextet related to hematite. The sample N3 shows only two doublets with $\delta = 0.29 \pm 0.01$ and 0.38 ± 0.01 mm s^{-1} related to Fe^{III} T_d and Fe^{III} O_h, respectively. These results show that Fe^{II} in the slag was oxidized to Fe^{III} upon dissolution in HNO_3 and drying, while hematite can be formed by heat treatment. On the other hand, the spectra and fitted parameters for the sample prepared by melt-quenching after heat treatment at 800 °C for 100 min, shown in Fig. 4(c) and Table 3, show two doublets with $\delta = 0.36 \pm 0.01$ and 0.34 ± 0.01 mm s^{-1}, related to Fe^{III} O_h, which is similar to $\delta = 0.38 \pm 0.04$ mm s^{-1} obtained for the sample prepared by melt-quenching reported in our previous paper [11]. The detection of hematite in the dissolved slag following heat treatment is interesting behaviour compared to melt-quenching, although both samples have the same total iron content. In our previous paper [11], where the samples were prepared using melt-quenching, hematite was detected by RT-Mössbauer only for the sample containing 50% Fe_2O_3. The existence of hematite in the dissolved slag was found to be effective for MB degradation, as will be discussed in degradation measurements section. This demonstrates the advantage of dissolving slag in HNO_3 over melt-quenching, to prepare an effective, low-cost photocatalyst. It is noticed that the hematite absorption peak decreases as the amount of HNO_3 decreased, where it was 33, 29 and 20% for N20, N10 and N5, respectively. This may be due to the lower amount of HNO_3 resulting in the incomplete dissolution of iron oxide in slag. As a result, a lower amount of iron nitrate may be formed, and consequently, the hematite, which results from thermal decomposition of iron nitrate, was decreased. This can be seen in the case of sample N3, for which no hematite was detected for the above-mentioned reason. The Mössbauer results are consistent with the XRD results.

3.1.2.2 Mössbauer spectroscopy of slag dissolved in diluted HNO_3

The spectra and fitted parameters for the samples dissolved in dilute HNO_3 (75 and 50%) before and after heat treatment at 800 and 1000 °C for 100 min are shown in Fig.

4(a), (b) and Table 4, respectively. Using diluted HNO_3 (with HNO_3 of 75%) resulted in hematite content with absorption peaks of 38 and 40% for the samples N5-75-1000 and N5-75-800 °C, respectively. Further decrease in HNO_3 concentration to 50% resulted in more hematite with absorption peaks of 33 and 50% for the samples N5-50-1000 and N5-50-800 °C, respectively. Compared to the hematite content (20%) in the case of the sample produced using concentrated HNO_3 (N5-1000), it can be observed that more dilute HNO_3 is more effective for obtaining high hematite contents in the final materials, which can enhance the photocatalyst performance. This can be explained by the hydrolysis being affected by the ratio of water in the solution. Before heat treatment, both samples show two doublets related to Fe^{III} O_h with $\delta = 0.37 \pm 0.02$ and 0.57 ± 0.04 mm s^{-1} for N5-75, $\delta = 0.36 \pm 0.01$ and 0.39 ± 0.05 mm s^{-1} for N5-50, respectively, indicating the oxidation of Fe^{II} in the slag to Fe^{III} after drying, however, heat treatment is required for the formation of hematite. To obtain more investigation about the effect of heat treatment temperature on the obtained hematite, the sample N5-50 was heat-treated at 600 °C for 100 min. From Mössbauer measurements shown in Fig 4(c) and Table 4, only two doublets were obtained with $\delta = 0.32 \pm 0.01$ and 0.35 ± 0.02 mm s^{-1} and assigned as Fe^{III} T_d and Fe^{III} O_h, respectively, with no hematite detected. These results show that, of those temperatures studied here, the most effective heat treatment temperature to obtain hematite is 800 °C.

3.1.3. Morphology

Fig. 5 (A, B) show the SEM and TEM images of the samples N5-75 and N5-50 heat-treated at 800 and 1000 °C, respectively. From SEM images, all samples show uneven surfaces with different sizes and morphologies. The size and morphology are smaller, more porous and uniform in the case of lower heat-treated samples N5-75-800 and N5-50-800 compared to higher heat-treated samples N5-75-1000 and N5-50-1000. The average aggregate' sizes are 4.2, 5.4, 3.9, and 4.4 μm for N5-75-800, N5-75-1000, N5-50-800 and N5-50-1000, respectively. Average aggregate' sizes are lower in the case of lower heat-treatment which is an advantage for using these samples in practical applications. The TEM images give a more clear analysis of these samples, for which the

particle size for N5-75-800 varies from 5 to 9 nm, having the smallest particle size among all samples studied. For sample N5-75-1000, the particle size has grown slightly to approximately 12 nm. The sample N5-50-800 has particles with a size approximately 21 nm while sample N5-50-1000 exhibits particles with sizes varies from 15 to 24 nm. These larger particle sizes for samples heat-treated at 1000 °C are consistent with their higher heat treatment temperatures.

3.2. Photocatalytic properties

3.2.1. Photo-Fenton reaction for the concentrated HNO_3 treated samples

The results of MB degradation under the photo-Fenton reaction of the heat-treated samples N20, N10, N5 and N3 (see Fig. 6) show that the degradation and *k* values increase with the amount of HNO_3 used for dissolving the slag. This trend can be explained by considering the structural characterization from both XRD and Mössbauer spectroscopy; it is correlated with the amount of hematite in the sample. The apparent *k* values for the samples N20, N10, N5 and N3 were (8.1 ± 0.2, 5.0 ± 0.2, 3.0 ± 0.1 and 1.4 ± 0.1) $\times 10^{-2}$ min^{-1} after 60 min of irradiation where the hematite contents were 33%, 29%, 20% and zero, respectively. To clarify the greater effectiveness of this method over melt-quenching, another sample was prepared by melt-quenching using the same collected slag, and then heat-treated at 800 °C for 100 min. The MB test for this sample resulted in a *k* value of $2.2 \pm 0.1 \times 10^{-2}$ min^{-1} after 3h of irradiation. These results show that the acid dissolution and heat treatment method resulted in cost-effective visible light photocatalysts also reducing the time required for the MB degradation from 3h to 1h. The degradation of the blank sample (without catalyst) and dark samples (measured in the dark) have small *k* values of (0.25 ± 0.01, 0.28 ± 0.01, 0.25 ± 0.01, 0.21 ± 0.01, and 0.10 ± 0.01) $\times 10^{-2}$ min^{-1}, respectively, which means that the degradation is due mainly to photoactivity rather than photolysis or adsorption. The advantage of the photo-Fenton reaction over photoactivity can be clarified by measuring all samples under the same conditions without applying the photo-Fenton reaction. The *k* values for samples N20, N10, N5 and N3 were (1.32 ± 0.03, 1.01 ± 0.02, 0.48 ± 0.01 and 0.3 ± 0.01) $\times 10^{-2}$ min^{-1},

respectively, which are far smaller compared to *k* values from the photo-Fenton reaction, however, it has the same trend in variation of *k* as a function of hematite content.

3.2.2. Photo-Fenton reaction for the diluted HNO_3 treated samples

We aimed to prepare a cost-effective catalyst so the *k* / acid ratio was calculated to choose the most practical sample. From these results, shown in Fig. 6 inset, sample N5 was chosen since it provided the highest *k* / acid ratio. The amount of HNO_3 was diluted with distilled water to 75, 50 and 25%. The slag could not be fully dissolved at the low HNO_3 concentration of 25% so two samples denoted as N5-75 and N5-50 were obtained for the corresponding HNO_3 concentrations of 75 and 50%, respectively. Both samples were heat-treated at 1000 and 800 °C according to the TG results (see Fig. 1) and denoted as samples N5-75-1000, N5-75-800, N5-50-1000 and N5-50-800, respectively. The photo-Fenton measurements for these samples are shown in Fig. 7, and the results can be summarized as follows:

Firstly, the *k* values in the case of samples N5-75-1000 and N5-75-800 were $(3.9 \pm 0.1$ and $4.5 \pm 0.1) \times 10^{-2}$ min^{-1}, respectively, while for samples N5-50-1000 and N5-50-800 it was $(3.4 \pm 0.1$ and $4.1 \pm 0.1) \times 10^{-2}$ min^{-1}, respectively. The higher *k* values in the case of higher acid content indicate that the slag / acid ratio plays a major role in the effectiveness of the prepared catalyst.

Secondly, the results of photo-Fenton reactions are correlated with the hematite content of the sample. The Mössbauer absorption area (Table 4) for sample N5-50-800 was detected to be 50%, having a *k* value of $(4.1 \pm 0.1) \times 10^{-2}$ min^{-1} while absorption area was 33% for sample N5-50-1000 with a lower *k* value of $(3.9 \pm 0.1) \times 10^{-2}$ min^{-1}. The same trend can be observed for the sample N5-75 although the difference in the absorption area is not large (40% for 800 °C and 38% for 1000 °C) but it is also important to consider the additional doublet for the sample prepared at 800 °C with the octahedral site and absorption area of 10%.

Thirdly, for each sample, it can be seen that the lower heat treatment temperature resulted in higher MB degradation. This can be an indication of particle size (and

therefore higher surface area) contribution where the particle size is larger in the higher temperature samples. From XRD shown in Fig. 2(a) and (b), it can be observed that both samples N5-75-1000 and N5-50-1000 produce sharp diffraction peaks with narrow full-width, half-maximum (FWHM) line widths compared to XRD patterns for samples N5-75-800 and N5-50-800. Sharp diffraction peaks correspond to larger crystallite size, which is reflected in the surface area, an important parameter for effective photocatalysts. To clarify the contribution of surface area and its relation to MB degradation, the surface areas of these samples were measured. The BET results (Table 5) clearly show that the surface area has a positive correlation with MB degradation, where it is larger in the case of higher HNO_3 content and low heat treatment temperature, (3.64 and 5.38 m^2 / g) for samples N5-75-1000 and N5-75-800 compared to the lower HNO_3 content (2.16 and 2.63 m^2 / g) for samples N5-50-1000 and N5-50-800, respectively.

Fourthly, the sample prepared by melt-quenching has a *k* value of $(2.2 \pm 0.1) \times 10^{-2}$ min^{-1} which is almost half of that for the HNO_3 produced samples. By considering the structural analysis of this sample, it can be seen that it produces only Mössbauer doublets and no hematite sextets, and thus no hematite can be observed by either XRD Fig. 2(c) or Mössbauer spectroscopy Fig. 4(c). This may be the reason for the low *k* value obtained for this sample in addition to the fact that the melt-quenching method results in lower surface area.

Fifthly, before heat treatment, the photoactivity of both samples N5-75 and N5-50 were measured. It was found that they produce much higher MB degradation than the heat-treated samples, with 88% of MB removal for both samples after only 20 min. Both samples were measured in dark conditions and also provide high MB degradation of 68% and 61% after 20 min for samples N5-75 and N5-50, respectively. These values were mainly due to the effect of adsorption and homogeneous Fenton reaction rather than the photo-Fenton reaction. Iron nitrate salts (present in the samples before heat treatment) accompanied by low pH (due to the presence of HNO_3 which is not completely removed after drying at 80 °C) are a good environment for the homogeneous Fenton reaction. The sample N5-50 was heat-treated at 600 °C for 100 min and shows a lower *k* value of $(1.5 \pm 0.1) \times 10^{-2}$ min^{-1} compared to sample N-5-50-800. By considering the fitted Mössbauer parameters for this sample (Table 4), the spectra are composed of two

doublets with δ = (0.35 ± 0.02 and 0.32 ± 0.01) mm s^{-1} assigned as Fe^{III} O_h and Fe^{III} T_d, respectively, where hematite is not detected (lack of sextet), which confirms that hematite plays the major role in the MB degradation and it can be obtained only by heat treatment at 800 ℃.

3.2.3. Parameters affecting MB degradation

The sample N5-50-800 has lower acid content and lower heat treatment temperature, hence, it was chosen for further study.

a- Effect of H_2O_2

The oxidation of organic pollutants using Fenton reactions is strongly dependent on the addition of H_2O_2 because it controls the generation of active radicals. The MB degradation has been studied under a range of H_2O_2 concentrations (0.1 to 1.6 M); the results are shown in Fig. 8(a). By increasing the H_2O_2 concentration from 0.1 to 0.35 M the degradation increases from 70.3% to 90.6% removal of MB where more H_2O_2 produces more active radicals [22]. However, excess H_2O_2 decreases the degradation from 90.6% to 80.8%, mostly because it acts as a scavenger of hydroxyl radicals [22, 23]. Also, more H_2O_2 can generate more $^{\cdot}OH$, which can be dimerized to form H_2O_2 so cumulative effects can inhibit the MB degradation. The excess of H_2O_2 may also encourage the formation of less active hydroperoxyl radicals which can react with hydroxyl radicals to form water [24]. The best-performing H_2O_2 concentration was found to be 0.35 M, which produced a k value of 4.1×10^{-2} min^{-1}.

b- Effect of MB concentration

Dye concentration affects the intensity of light passing through the reaction medium to reach the surface of the photocatalyst. The photodegradation of MB was conducted under initial concentrations of 20, 40 and 60 μM. MB degradation is shown in Fig. 8(b) and displays an inverse relation with the initial concentration, where it was 90.6%, 69.2% and 65.5% for MB of 20, 40 and 60 μM after 60 min of irradiation, respectively. This can

be attributed to the decrease in $^{\cdot}OH$, radical generation due to the coverage of catalyst active sites by the adsorbed dye [24, 25]. Moreover, the intermediate compounds formed during the degradation process increase with the increase in the initial dye concentration and might consume some active radicals that are supposed to react with the dye molecules [26].

c- Effect of catalyst loading

Determining the optimum catalyst loading is essential in photodegradation reactions, since it helps in consequently scaling up the photocatalytic process, thereby affecting the economics of the whole process. This includes the production cost which should be minimized. Not only this but also catalyst recovery after the end of the reaction must be considered. In our case, the prepared catalyst (iron silicate powder) loading was varied from 2 to 24 g L^{-1}. The results of MB degradation measured after 60 min as a function of the catalyst loading are presented in Fig. 8(c). Increase in the MB degradation was observed, from 84.4% for 2 g L^{-1} to 90.6% for 4 g L^{-1}. This increase in degradation is due to the increase in the active surfaces for the same unit volume of MB [24], which will lead to an increase in the absorbed photons and consequently in the generation of $^{\cdot}OH$ radicals which initiate the reaction [25]. Further increase leads to a decrease in MB degradation from 90.6% for 4 g L^{-1} to 81.8% for 24 g L^{-1}, mostly caused by a reduction in light intensity as the solution opacity increases [27, 28]. It is also possible that at higher catalyst loading, the iron act as a scavenger and reacts with $^{\cdot}OH$ radicals [24]. The optimum catalyst loading was found to be 4 g L^{-1}.

d- Effect of temperature

The reaction temperature is a critical operating parameter. Fig 8(d) shows the influence of the reaction temperature on MB removal. The experiments were performed at four different temperatures, namely, 303K, 313K, 323K, and 333K. It can be seen that with increasing temperature, the rate of the reaction increases from 4.1×10^{-2} min^{-1} at 303K to 13.0×10^{-2} min^{-1} at 333K. The increase in temperature increases interaction of

the hydroxyl radicals and the dye molecules and the reaction competes more efficiently with electron-hole recombination [11, 28].

The activation energy (E_a), estimated using the rate constants (k_t) from the Arrhenius equation [22], were calculated according to Eq. (1)

$$\ln k_t = - E_a/RT + \ln A \quad (1)$$

Where k_t is the reaction rate constant as a function of temperature; E_a ($J \cdot mol^{-1}$) is the apparent activation energy; R is the universal gas constant of 8.314 $J \cdot mol^{-1} \cdot L^{-1}$; T (K) is the absolute temperature; A is the Arrhenius pre-exponential factor

The apparent activation energy of MB obtained in this study Fig. 8(d) (inset) was 31.5 $KJ.mol^{-1}$ which is higher than values obtained from other studies reported by Okamoto [29] for the photodegradation of phenol (10.0 kJ / mole) and by Al-Sayyed [30] for the degradation of 4-chlorophenol (5.4 kJ / mole). The high value obtained in this study suggests that thermal activation is important to accelerate the photo-degradation [31].

e- Effect of pH

The pH is considered the main parameter affecting the adsorption/desorption processes due to its impact on the surface charge of the catalyst. This affects the adsorption of reactants and dye molecules on the surface of the catalyst, and desorption of the reaction products back into solution [26]. The effect of the solution pH within the range of 3 to 11 on the degradation efficiency was investigated; the results are presented in Fig. 9. An increase in the degradation efficiency was observed with increasing pH from 3 to 11. At pH 11 the MB degradation is highest at 93.8% in 20 min, while the maximum degradation at lower pH was 32.2% and 80.5 % for pH of 9 after 20 and 60 min, respectively. The pH of the solution can enhance the degradation and ensure strong adhesion of dye molecules on the surface of the catalyst. This depends on the nature of

the dye (cationic, anionic or neutral). In our case, MB, which is a cationic dye, will be adsorbed more quickly at higher pH and consequently, an increase in the MB degradation rate is expected [25, 26]. The alkaline medium can also facilitate the formation of ^{-}OH ions which are responsible for the generation of $^{\cdot}OH$ radicals; this will lead to an increase in photodegradation rate [32]. It was reported that in acidic solutions, the surfaces of photocatalysts are positively charged while they are negatively charged in alkaline solutions [33]. As a result, the efficiency of MB photodegradation is expected to increase with pH, owing to electrostatic interactions between the negative surface and the MB cations.

To understand the influence of the solution pH on the Fenton process, the point of zero charge (PZC) of the N-5-50-800 sample was estimated (Inset Fig. 9). The obtained PZC value of 10.6 suggests that the surfaces of the catalyst were negatively charged at pH higher than 10.6, which is ideal for the degradation of the cationic MB due to electrostatic interactions [22]. The high value of PZC explains the rapid increase in the degradation from 32.2% to 93.8% for pH of 11 and 9 after 20 min, respectively.

3.2.4. Stability and Recyclability

Catalyst recyclability is an increasingly important feature of catalysts for industrial applications. In this study, the reusability of the best-performing sample, N5-50-800, was tested at an initial pH of 11. Fig. 10 illustrates the relationship between MB degradation efficiency and the number of cycles, tested at 20 min of irradiation after 7 successive cycles where the degradation was decreased by only 6.3%. The repeated measurements were carried out by centrifuging the solution followed by removing and replacing it with a new MB solution. No further filtration or drying of the powder was carried out between subsequent experiments, which can further lower the operational cost if the catalyst were applied in a large-scale process.

Conclusions

A visible light photocatalyst was successfully prepared by dissolving the combustible waste slag in nitric acid. The photocatalytic activity of the prepared samples was found to

obey the pseudo-first-order rate constant, having a *k*-value of $(4.1 \pm 0.1) \times 10^{-2}$ min^{-1} for sample N5-50-800 in the photo-Fenton process. The *k*-value increased to $(1.4 \pm 0.1) \times 10^{-1}$ min^{-1} for the same sample after controlling the initial pH to 11. The sample prepared by the melt-quenching method using the same slag has a maximum *k* value of $(2.2 \pm 0.1) \times 10^{-2}$ min^{-1} under the same conditions, which illustrates the effectiveness of the method used in this study. The obtained results of photocatalytic activity are correlated to the amount of hematite in each sample, as detected by XRD and ^{57}Fe Mössbauer measurements. It was found that the HNO_3 concentration and heat treatment temperature have a large impact on both hematite content and the surface area of the prepared samples and, consequently, on the methylene blue degradation ability. The optimum conditions for practical usage of the samples are using sample N5-50-800 in the photo-Fenton reaction with 0.35 M of H_2O_2, a catalyst (iron silicate powder) loading of 4 g L^{-1}, MB initial concentration 20 μM and initial pH of 11.

CRediT author statement:

Ahmed Salah Ali: Conceptualization, Methodology **Irfan Khan:** Writing-Reviewing and Editing **Bofan Zhang:** Methodology **Kiyoshi Nomura:** Software **Homonnay Zoltan:** Writing-Reviewing and Editing **Erno Kuzmann:** Writing-Orginal draft **Alex Scrimeshire:** Software **Paul Bingham:** Methodology **Stjepko Krehula:** Visualization **Svetozar Music:** Data curation **Kazuhiko Akiyama:** Data curation **Shiro Kubuki:** Supervision.

Declaration on conflict of interests

The authors declare that they have no known competing financial interests or personal relationships that could have appeared to influence the work reported in this paper.

Acknowledgements

Some of the authors (ASA, KN, KA, SK) express their gratitude for the financial support from Tokyo Human Resources Fund for City Diplomacy, Grant Number H29-1. We are also thankful to Prof. Tetsuya Shishido and Mr Kenji Aihara of Tokyo Metropolitan University, Japan, for their support in this work.

554

555 ## References

556 [1] Ferronato N, Torretta V (2019) Waste mismanagement in developing countries: A
557 review of global issues. Int. J. Environ. Res. Public Health 16:1–28
558 [2] Mary Joseph A, Snellings R, Heede P V d, Matthys S, Belie N.D (2018) The use of
559 municipal solid waste incineration ash in various building materials: A Belgian point
560 of view. Materials 11:1–30
561 [3] Yildirim I Z, Prezzi M (2011) Chemical, mineralogical and morphological properties
562 of steel slag. Adv. Civ. Eng. 2011:1–13
563 [4] Perrot J F, Alison Subiantoro A (2018) Municipal waste management strategy review
564 and waste-to-energy potentials in New Zealand. Sustainability 10:1–12
565 [5] Ishikawa S, Kobzi B, Sunakawa K, Nemeth S, Lengyel A, Kuzmann E, Homonnay
566 Z, Nishida T, Kubuki S (2017) Visible-light activated photocatalytic effect of glass
567 and glass ceramic prepared by recycling waste slag with hematite. Pure Appl. Chem.
568 89: 535–554
569 [6] Fujishima A, Honda K (1972) Electrochemical photolysis of water at a
570 semiconductor electrode. Nature 238:37-38
571 [7] Koehl M, Philipp D, Lenck N, Zundel M (2009) Development and application of a
572 UV light source for PV-module testing. Proc. of SPIE 7412:1–7
573 [8] Aramyan S, Moussavi M (2017) Advances in Fenton and Fenton Based Oxidation
574 Processes for Industrial Effluent Contaminants Control-A Review. Int. J Environ.
575 Sci. Nat. Res. 2:1–18
576 [9] Iida Y, Akiyama K, Kobzi B, Sinkó K, Homonnay Z, Kuzmann E, Ristić M, Krehula
577 S, Nishida T, Kubuki S (2015) Structural analysis and visible light-activated
578 photocatalytic activity of iron-containing soda lime aluminosilicate glass. J. Alloys.
579 Comp. 645:1–6
580 [10] Khan I, Nomura K, Kuzmann E, Homonnay Z, Sinkó K, Ristić M, Krehula S,
581 Musić S, Kubuki S (2020) Photo-Fenton catalytic ability of iron-containing
582 aluminosilicate glass prepared by sol-gel method. J. Alloys. Comp. 816:1–7

583 [11] Ali A S, Nomura K, Homonnay Z, Kuzmann E, Scrimshire A, Bingham P A,
584 Krehula S, Ristić M, Musić S, Kubuki S (2019) The relationship between local
585 structure and photo‐Fenton catalytic ability of glasses and glass‐ceramics prepared
586 from Japanese slag. J. Radioanal. Nuc. Chem. 322:751–761

587 [12] Melnikov P, Nascimento V A, Arkhangelsky I V, Zanoni Consolo L Z, de Oliveira L
588 C S (2014) Thermal decomposition mechanism of iron (III) nitrate and
589 characterization of intermediate products by the technique of computerized
590 modeling. J Therm. Anal. Calorim. 115:145–151

591 [13] Machulek A, Quina F, Gozzi F, Silva V, Friedrich L, Moraes J (2012) In: Puzyn T
592 (ed) Organic pollutants ten years after the Stockholm convention—environmental
593 and analytical update, 1st edn. Intechopen, London
594 [14] Akcil A, Karshigina Z B, Bochevskaya Ye G, Abisheva Z S (2018) Conditions of
595 nitric acid treatment of phosphorus slag from REMs recovery and production of
596 precipitated silicon. Metallurgy 2:28–38
597 [15] Du C, Gao X, Ueda S, Kitamura S (2016) Effects of Cooling Rate and Acid on
598 Extracting Soluble Phosphorus from Slag with High P_2O_5 Content by Selective
599 Leaching. ISIJ International 510:1–10
600 [16] Zhang Y, He P. Chen H (2018) A novel CdO/graphene alkali-activated steel slag
601 nanocomposite for photocatalytic degradation of dye wastewater. Ferroelectrics
602 522:1–8
603 [17] Kang L, Zhang Y, Wang L, Zhang L, Zhang K, Liu L (2015) Alkali-Activated steel
604 slag-based besoporous material as a new photocatalyst for degradation of dye from
605 wastewater. Integr. Ferroelectr. 162:8–17
606 [18] Zeynolabedin R, Mahanpoor K (2017) Preparation and characterization of nano-
607 spherical $CoFe_2O_4$ supported on copper slag as a catalyst for photocatalytic
608 degradation of 2-nitrophenol in water. J. Nanostruct. Chem. 7:67–74
609 [19] Salgado S Y A, Pérez A A M, López M S, Zamora R M R (2016) Evaluation of
610 metallurgical slag as a Fenton-type photocatalyst for the degradation of an
611 emerging pulutent: Diclofenac. Catal. Today 266:126–135

612 [20] Gong X, Jia F, Liu R, Ye F, Guan H, Wang R, Guo G (2014) Study on preparation
613 and photocatalytic activity of photocatalyst made from Ti-bearing blast furnace slag.
614 Appl. Mech. Mater. 526:33–39
615 [21] Sun Y, Zhang J, Wang Y, Li Q (2016) Inhibitory Effect of Thioacetamide On CdS
616 Dissolution During Photocatalytic Oxidation of 2,4-Dichlorophenol. Rare Metal
617 Technology 1:87-88
618 [22] Saleh R, Taufik A (2019) Degradation of methylene blue and congo-red dyes using
619 Fenton, photoFenton, sono-Fenton, and sonophoto-Fenton methods in the presence
620 of iron (II,III) oxide/zinc oxide/graphene (Fe_3O_4/ZnO/graphene) composites. Sep.
621 Purif. Technol. 210:563-573
622 [23] Guo S, Zhang G, Wang J (2014) Photo-Fenton degradation of Rhodamine B using
623 Fe_2O_3–Kaolin as heterogeneous catalyst: Characterization, process optimization
624 and mechanism. J. Colloid Interf. Sci. 433:1-8
625 [24] Nasuh N, Ismail S, Hameed H (2016) Activated electric arc furnace slag as an
626 effective and reusable Fenton-like catalyst for the photodegradation of methylene
627 blue and acid blue 29. J. Taiwan Inst. Chem. E. 67:235–243
628 [25] Reza K M, Kurny A S W, Gulshan F (2017) Parameters affecting the photocatalytic
629 degradation of dyes using TiO_2: a review. Appl. Water Sci. 7:1569–1578
630 [26] Abdellah M H, Nosier S A, El-shazly A H, Mubarak A A (2018) Photocatalytic
631 decolorization of methylene blue using TiO_2/UV system enhanced by air sparging.
632 Alex. Eng. J. 57:3727–3735
633 [27] Soltani N, Saion E, Hussein M Z, Erfani M, Abedini A, Bahmanrokh G, Navasery
634 M, Vaziri P (2012) Visible light-induced degradation of methylene blue in the
635 presence of photocatalytic ZnS and CdS nanoparticles. Int. J. Mol. Sci., 13:12242–
636 12258
637 [28] Gajbhiye S B (2012) Photocatalytic degradation study of methylene blue solutions
638 and its application to dye industry effluent. IJMER 2:1204–1208
639 [29] Okamoto K, Yamamoto Y, Tanaka H, Tanaka M, Itaya A (1985) Heterogeneous
640 Photocatalytic Decomposition of Phenol over TiO_2 Powder. Bull. Chem. Soc. Jpn.
641 58: 2015-2022

[30] Al-Sayyed G, D'Oliveira J, Pichat P (1991) Semiconductor-sensitized photodegradation of 4-chlorophenol in water. J. Photochem. Photobiol. A: Chem. 58: 99–114

[31] Hu Q, Liu B, Zhang Z, Song M, Zhao X (2014) Temperature effect on the photoeatalytic degradation of methyl orange under UV-vis Light irradiation. Journal of Wuhan University of Technology-Mater. Sci. Ed. 25:210-213

[32] Kaur J, Bansal S, Singhal S (2013) Photocatalytic degradation of methyl orange using ZnO nanopowders synthesized via thermal decomposition of oxalate precursor method. Physica, B Condens. Matter 416:33–38

[33] Tang Z W, Huang C P (1995) Inhibitory Effect of Thioacetamide on CdS Dissolution During Photocatalytic Oxidation of 2, 4-Dichlorophenol. Chemospher 30:1385–1399

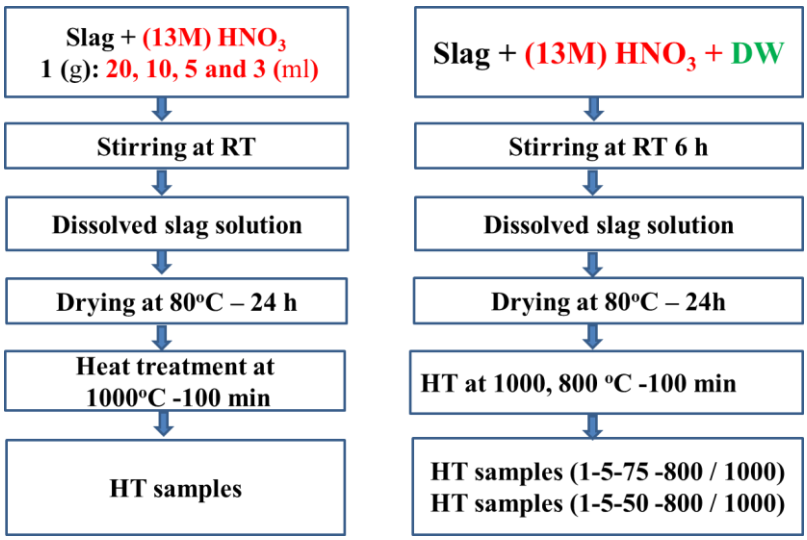

A. S. Ali *et al.*, Scheme 1

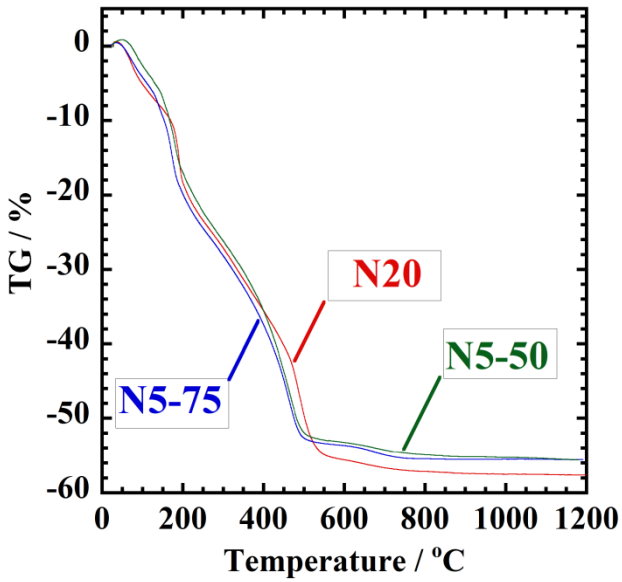

A. S. Ali *et al.*, Fig. 1

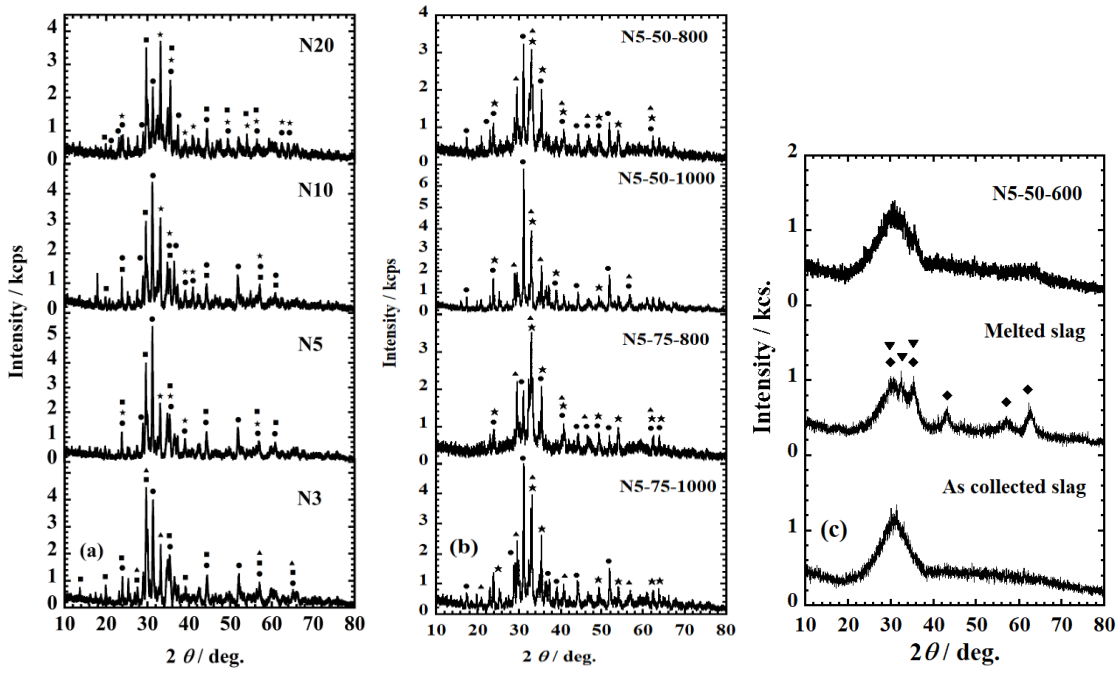

● **Gehlenite** ▲ **Andradite**
■ **Essenite** ◆**Iron silicon oxide**
★ ***α*-Fe_2O_3 (Hematite)** ▼ **Calcium silicate**

A. S. Ali *et al.*, Fig. 2 (a), (b), (c)

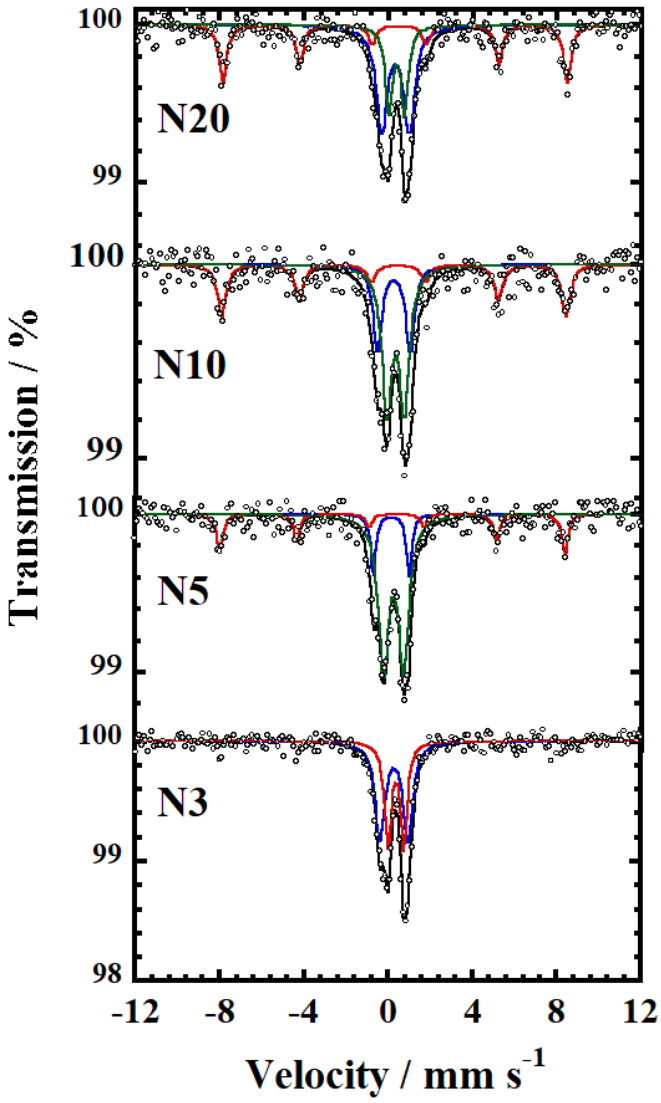

A. S. Ali *et al.*, Fig. 3

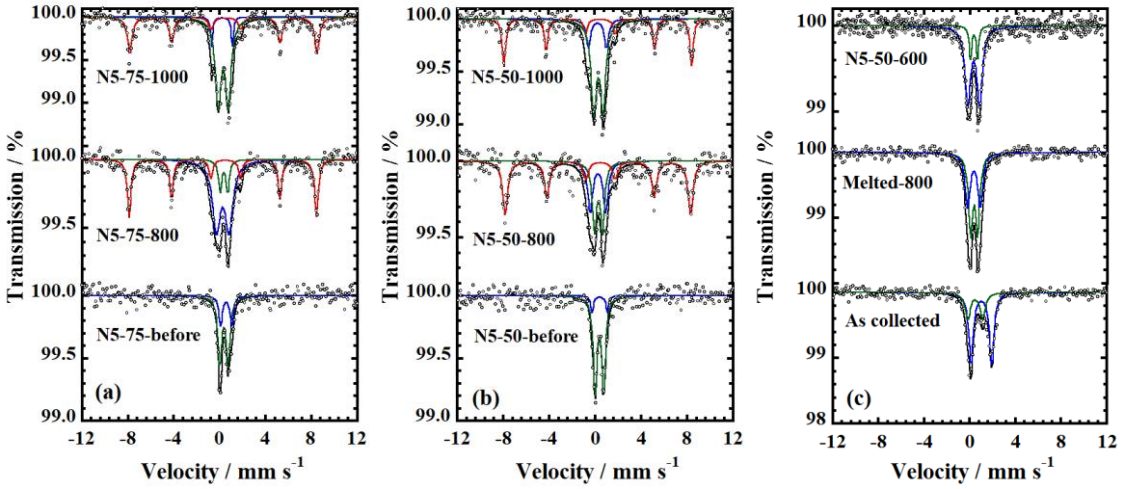

A. S. Ali *et al.*, Fig. 4 (a), (b), (c)

747

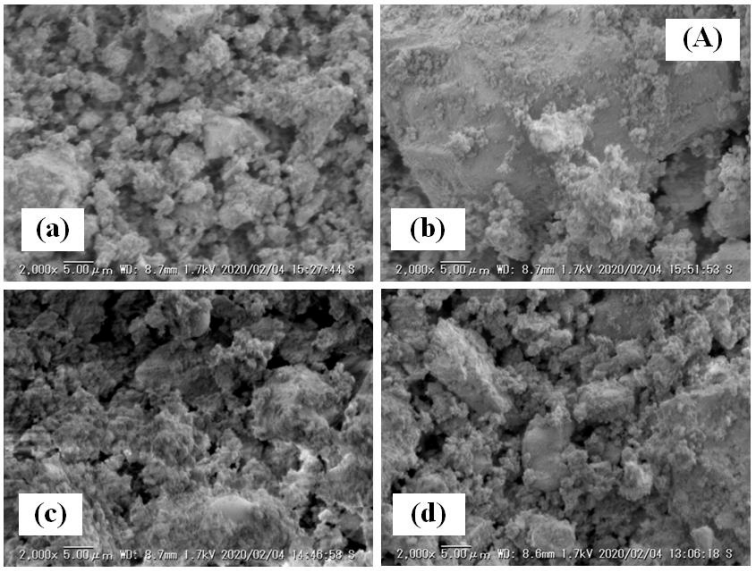

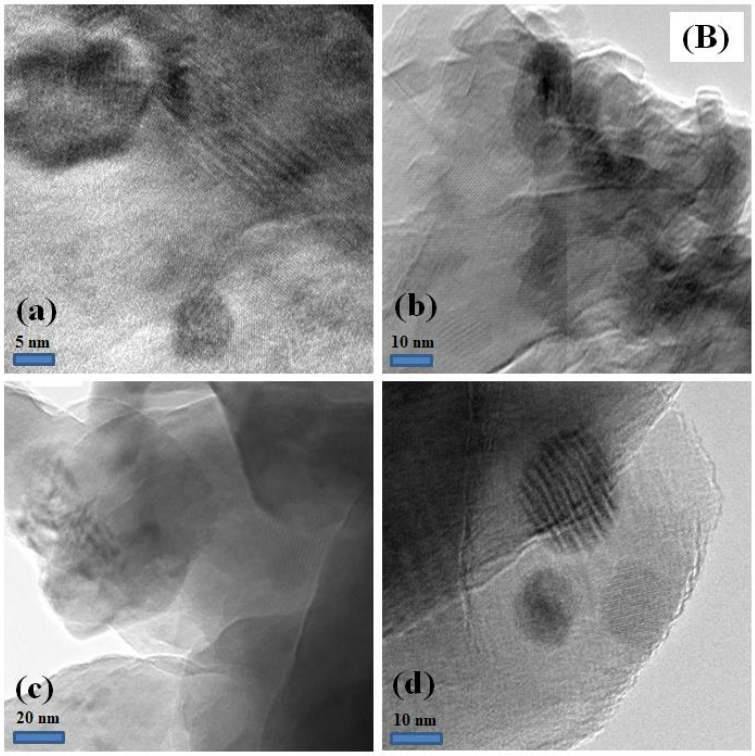

748
749

750

751

752 A. S. Ali *et al.*, Fig. 5

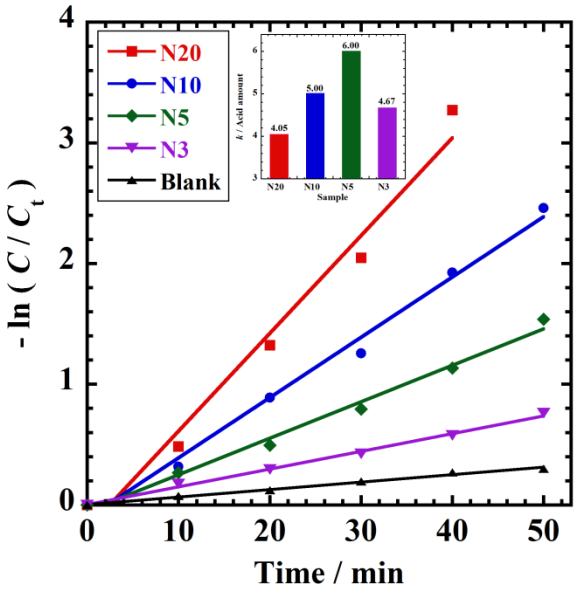

A. S. Ali *et al.*, Fig. 6

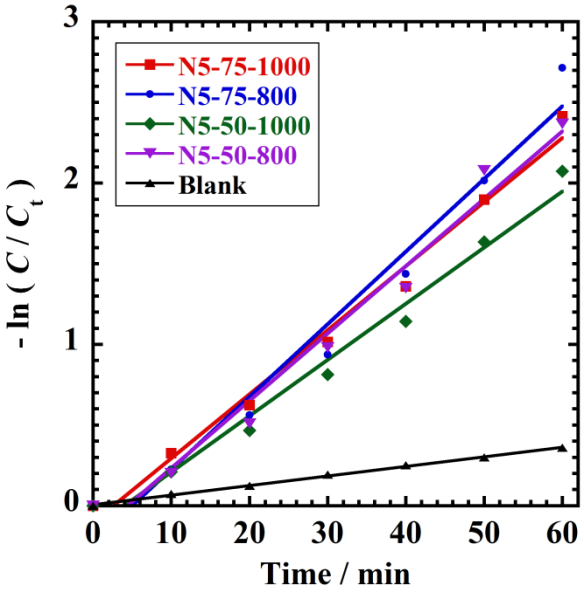

A. S. Ali *et al.*, Fig. 7

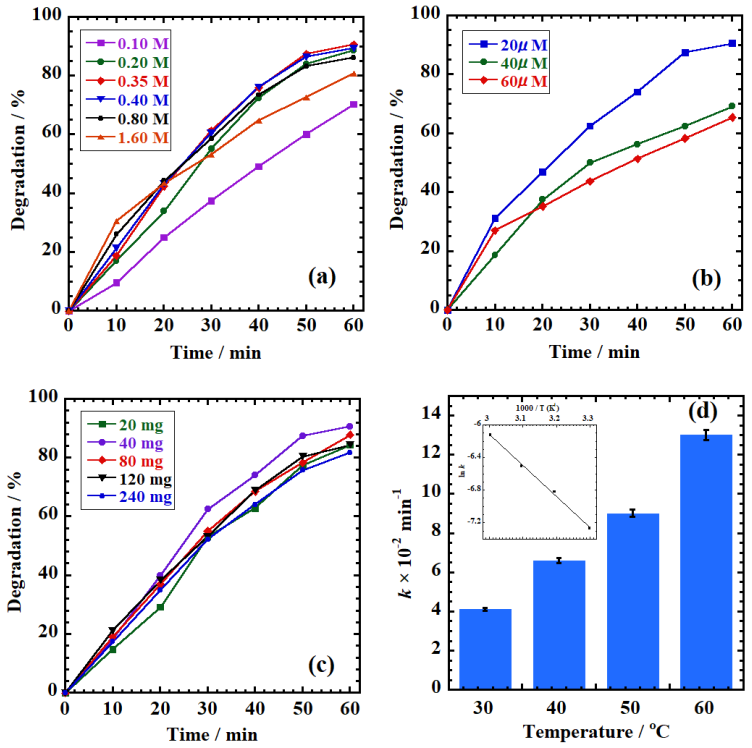

A. S. Ali *et al.*, Fig. 8 (a), (b), (c), (d)

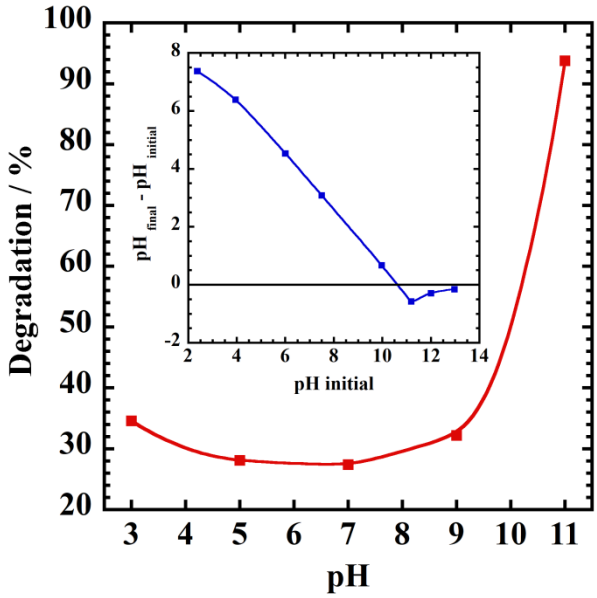

A. S. Ali *et al.*, Fig. 9

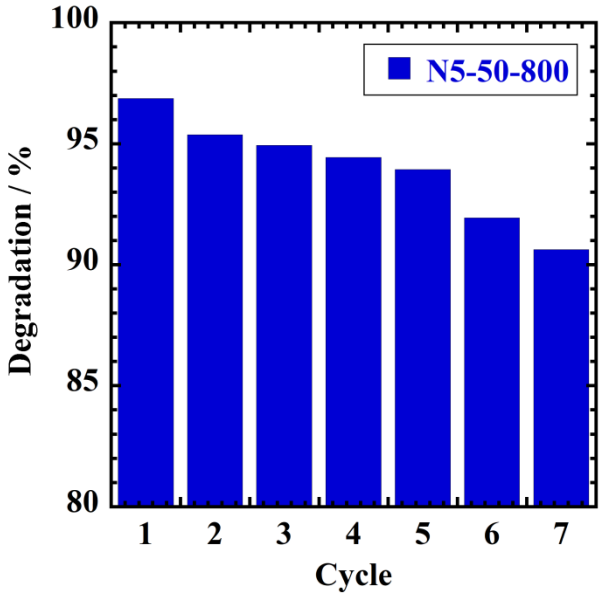

819
820
821
822
823
824
825
826
827
828
829
830
831
832
833
834
835 A. S. Ali *et al.*, Fig. 10

836 ## Figure Captions

837 **Scheme 1** Schematic diagram of the sample preparation using concentrated HNO_3 (left)

838 and diluted HNO_3 (right)

839 **Fig. 1** TG curves of the samples N20, N5-75 and N5-50

840 **Fig. 2** XRD patterns of samples (a) prepared using concentrated HNO_3 heat-treated at

841 1000 °C for 100 min, (b) prepared using diluted HNO_3 heat-treated at 800 and 1000 °C

842 for 100 min and (c) as collected slag, melted slag heat-treated at 800 °C for 100 min and
843 the sample prepared using diluted HNO_3 heat-treated at 600 °C for 100 min
844
845 **Fig. 3** RT Mössbauer spectra of samples prepared using concentrated HNO_3 heat-treated
846 at 1000 °C for 100 min
847
848 **Fig. 4** RT Mössbauer spectra of samples prepared using diluted HNO_3 (a) 75% (b) 50%
849 and (c) as collected slag, melted slag heat-treated at 800 °C for 100 min and the sample
850 prepared using diluted HNO_3 heat-treated at 600 °C for 100 min
851
852 **Fig. 5** Images of (A) SEM and (B) TEM of the samples (a) N5-75-800 (b) N5-75-1000
853 (c) N5-50-800 (d) N5-50-1000
854
855 **Fig. 6** Kinetic dye degradation measurements of methylene blue for the samples prepared
856 using concentrated HNO_3 heat-treated at 1000 °C for 100 min under photo Fenton the
857 inset is the ratio of *k* and acid amount for each sample
858
859 **Fig. 7** Kinetic dye degradation measurements of methylene blue for the samples prepared
860 using diluted HNO_3 heat-treated at 800 and 1000 °C for 100 min under photo Fenton
861
862 **Fig. 8** Effect of (a) H_2O_2 concentration, (b) MB concentration, (c) catalyst (iron silicate
863 powder) loading and (d) temperature on the MB degradation for the sample N5-50 heat-
864 treated at 800 ^oC for 100 min
865
866 **Fig. 9** Influence of pH on the MB degradation for the sample N5-50 heat-treated at 800
867 ^oC for 100 min the inset is zero point of charge
868
869 **Fig. 10** Reusability of the samples N5-50-800 for MB degradation at pH 11 under
870 catalyst loading 4 g/L, MB concentration 20 μM and H_2O_2 concentration 0.35M
871
872

Table 1 XRF compositional analysis of domestic waste slag (weight %) collected July 2018

O_3	Fe_2O_3	CaO	Na_2O	TiO_2	MgO	P_2O_5	K_2O	
30	18.33	24.61	4.69	2.14	3.12	1.45	0.21	

A. S. Ali *et al*

Table 2 Composition and identification of the samples dissolved in diluted HNO_3

Slag (g)	HNO_3 (ml)	DW (ml)	HNO_3 V (%)	Sample identification (Slag-Solution-HNO_3)
1.00	3.75	1.25	75	1-5-75
1.00	2.50	2.50	50	1-5-50
1.00	1.25	3.75	25	1-5-25

A. S. Ali *et al*

Table 3 Room temperature ^{57}Fe Mössbauer fitted parameters for room temperature analyses of as collected slag (not heat treated), slag melted at 1400 °C; heat treated at 800°C for 100 min; and concentrated HNO_3 dissolved slag samples after heat treatment at 1000°C for 100 min

Sample	Species	A (%)	δ (mm s^{-1})	Δ (mm s^{-1})	H_{int} (T)	Γ (mm s^{-1})
N20	Fe^{III} T_d	44	$0.33_{\pm 0.02}$	$1.30_{\pm 0.10}$	-	$0.63_{\pm 0.05}$
	Fe^{III} O_h	23	$0.39_{\pm 0.02}$	$0.74_{\pm 0.06}$	-	$0.40_{\pm 0.09}$
	Hem	33	$0.42_{\pm 0.02}$	$-0.20_{\pm 0.03}$	$50.6_{\pm 0.1}$	$0.42_{\pm 0.05}$
N10	Fe^{III} T_d	25	$0.25_{\pm 0.03}$	$1.55_{\pm 0.16}$	-	$0.48_{\pm 0.17}$
	Fe^{III} T_d	46	$0.34_{\pm 0.03}$	$0.82_{\pm 0.12}$	-	$0.56_{\pm 0.10}$
	Hem	29	$0.37_{\pm 0.02}$	$-0.23_{\pm 0.05}$	$50.6_{\pm 0.17}$	$0.48_{\pm 0.08}$
N5	Fe^{III} T_d	13.7	$0.15_{\pm 0.02}$	$1.69_{\pm 0.04}$	-	$0.29_{\pm 0.07}$
	Fe^{III} T_d	66	$0.26_{\pm 0.01}$	$0.95_{\pm 0.03}$	-	$0.58_{\pm 0.03}$
	Hem	20.3	$0.35_{\pm 0.03}$	$-0.21_{\pm 0.05}$	$50.7_{\pm 0.2}$	$0.35_{\pm 0.08}$
N3	Fe^{III} T_d	57.5	$0.29_{\pm 0.01}$	$1.33_{\pm 0.04}$	-	$0.53_{\pm 0.13}$
	Fe^{III} O_h	42.5	$0.38_{\pm 0.01}$	$0.76_{\pm 0.02}$	-	$0.37_{\pm 0.03}$
Melted slag	Fe^{III} O_h	55.6	$0.36_{\pm 0.01}$	$0.62_{\pm 0.06}$	-	$0.44_{\pm 0.05}$
	Fe^{III} T_d	44.4	$0.34_{\pm 0.01}$	$1.10_{\pm 0.09}$	-	$0.51_{\pm 0.06}$
As collected slag	Fe^{II} O_h	70.2	$1.01_{\pm 0.01}$	$1.81_{\pm 0.02}$	-	$0.47_{\pm 0.03}$
	Fe^{III} O_h	29.8	$0.48_{\pm 0.06}$	$1.32_{\pm 0.09}$	-	$0.53_{\pm 0.09}$

Hem. Hematite, T_d tetrahedral, O_h octahedral, A absorption area, δ isomer shift, Δ quadrupole splitting, H_{int} internal magnetic field, Γ line width

A. S. Ali *et al*

Table 4 Room temperature ^{57}Fe Mössbauer fitted parameters for room temperature analyses of diluted HNO_3 dissolved slag samples before and after heat treatment at 600, 800 and 1000°C for 100 min

Sample	Species	A (%)	δ (mm s^{-1})	Δ (mm s^{-1})	H_{int} (T)	Γ (mm s^{-1})
N5-50-1000	Fe^{III} T_d	13.6	0.24 ± 0.01	1.58 ± 0.06	-	0.46 ± 0.07
	Fe^{III} T_h	52.4	0.32 ± 0.01	0.80 ± 0.02	-	0.56 ± 0.04
	Hem	34.0	0.37 ± 0.01	–0.23 ± 0.03	50.7 ± 0.1	0.35 ± 0.04
N5-50-800	Fe^{III} T_d	23.4	0.28 ± 0.03	1.36 ± 0.1	-	0.52 ± 0.1
	Fe^{III} T_d	27.0	0.32 ± 0.02	0.69 ± 0.08	-	0.45 ± 0.08
	Hem	49.6	0.39 ± 0.02	–0.23 ± 0.04	50.1 ± 0.1	0.53 ± 0.07
N5-50-600	Fe^{III} T_d	84.0	0.32 ± 0.01	1.04 ± 0.06	-	0.58 ± 0.03
	Fe^{III} O_h	16.0	0.35 ± 0.02	0.62 ± 0.05	-	0.25 ± 0.08
N5-50-bef	Fe^{III} O_h	88.7	0.36 ± 0.01	0.74 ± 0.04	-	0.38 ± 0.04
	Fe^{III} O_h	10.3	0.39 ± 0.05	1.32 ± 0.14	-	0.27 ± 0.03
N5-75-1000	Fe^{III} T_d	7.1	0.20 ± 0.02	1.81 ± 0.06	-	0.22 ± 0.08
	Fe^{III} T_d	54.5	0.30 ± 0.01	0.88 ± 0.03	-	0.60 ± 0.04
	Hem	38.3	0.43 ± 0.02	–0.22 ± 0.03	50.6 ± 0.10	0.48 ± 0.06
N5-75-800	Fe^{III} O_h	9.9	0.36 ± 0.04	0.65 ± 0.06	-	0.33 ± 0.10
	Fe^{III} T_d	50.3	0.26 ± 0.02	1.10 ± 0.10	-	0.81 ± 0.06
	Hem	39.8	0.39 ± 0.01	–0.25 ± 0.02	50.6 ± 0.07	0.38 ± 0.03
N5-75-bef	Fe^{III} O_h	72.4	0.37 ± 0.02	0.73 ± 0.04	-	0.40 ± 0.05
	Fe^{III} O_h	27.6	0.57 ± 0.04	0.97 ± 0.08	-	0.34 ± 0.1

Hem. Hematite, T_d tetrahedral, O_h octahedral, A absorption area, δ isomer shift, Δ quadrupole splitting, H_{int} internal magnetic field, Γ line width

A. S. Ali *et al*

Table 5 Surface area and *k* values of the samples prepared using diluted HNO_3 and heat treated at 800 and 1000 ^{o}C for 100 min

Sample	Surface area (m^2 / g)	k ($\times 10^{-2}$ min^{-1})
N5-50-800	2.63 ± 0.05	4.1 ± 0.1
N5-50-1000	2.16 ± 0.05	3.4 ± 0.1
N5-75-800	5.38 ± 0.10	4.5 ± 0.1
N5-75-1000	3.64 ± 0.07	3.9 ± 0.1

A. S. Ali *et al*